Sustainable Energy, Grids and Networks 32 (2022) 100955

Contents lists available at ScienceDirect

Sustainable Energy, Grids and Networks

journal homepage: www.elsevier.com/locate/segan

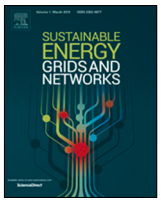

An active primary frequency regulation strategy for grid integrated wind farms based on model predictive control☆

Zhengyang Hu, Bingtuan Gao *, Ruizhe Sun

School of Electrical Engineering, Southeast University, Nanjing, China

ARTICLE INFO

Article history:
Received 19 April 2022
Received in revised form 10 October 2022
Accepted 6 November 2022
Available online 11 November 2022

Keywords:
Primary frequency regulation
Wind farm
Model predictive control
Small-signal analysis
Lyapunov stability

ABSTRACT

The increasing penetration level of wind power can reduce the dependency on fossil fuels, but it is accompanied with challenges such as the jeopardized dynamic stability of the frequency of power grid. As an effective method to improve frequency dynamic stability, primary frequency regulation (PFR) is conventionally based on the feedback of measured frequency, by which means it is conducted through analyzing historical information. By taking the predictive information into account, this paper introduces an active PFR (APFR) strategy for grid integrated wind farms (WFs) to enhance control performance of PFR. According to small-signal models of power system integrated with WFs based on conventional PFR and APFR, the state-space predictive models are established to obtain the predictive states. Then, to take active measures to deal with the electrical load disturbance, the predicted frequency is optimized in a receding horizon period by adjusting the PFR power reference of WFs flexibly. Moreover, a finite terminal weighting matrix based Lyapunov function is presented to prove the asymptotic stability of the closed-loop model predictive control system. Finally, extensive case studies based on the standard test systems are performed to validate the effectiveness of the theoretical analysis and the superiority of APFR strategy.

1. Introduction

Wind power is developed as one of the most promising sustainable energy sources to relieve the energy shortage and to solve environmental issues in recent years [1–3]. Integrating wind power in modern power system will decrease the reliance on fossil fuels and improve the reliability of the system. However, the high penetration of wind power will decrease the frequency regulation capacity inherently provided by the conventional synchronous generators (SGs), because the operation of wind turbines (WTs) is usually based on the maximum power point tracking (MPPT) technique, a technique that is decoupled from power system and does not respond to the system frequency deviation. As a consequence, more challenges rise to the power system frequency stability [4,5]. Therefore, as China has made it mandatory that WTs participate in primary frequency regulation (PFR), it is necessary to utilize the frequency support ability of WTs to achieve the goals of carbon emission peak and carbon neutrality.

Generally speaking, conventional SGs have reserved enough capacity for PFR, but the governor, high pressure cylinder and other mechanical parts in SGs often respond slowly in this area. On the contrary, WTs are integrated into power system via converters with the ability to adjust the power output quickly, but the output of which is unstable due to the randomness and intermittence of wind sources. Therefore, PFR strategies are proposed in [6,7] by releasing the kinetic energy stored in WTs. However, the virtual inertia and frequency droop control do not regulate the mechanical power captured by WTs. Besides, after a temporary frequency response, WTs have to absorb energy from the grid to recover back to the MPPT operation, which could cause the secondary frequency drop in power system. To address this issue, the deloading control is developed so that a certain amount of reserved power can be utilized in case of frequency events [8]. In [9], the over-speed control by shifting the MPPT curve to the right suboptimal curve is adopted in the deloading operation. Furthermore, the coordinated pitch control for PFR in case of over-speed control is presented [10], so that the captured wind energy of WTs can be regulated in both low and high wind speed condition.

Currently, the existing investigations on PFR strategies for wind power focus on the optimization of gain coefficient [11,12] and on the coordinated control of wind farms (WFs) [13,14]. The conventional PFR (CPFR) is designed to deal with the electrical load disturbance with short fluctuation period. The system frequency deviation can be restrained by controlling the power output of generators, and the active power variation of WTs is

☆ This work was supported by National Key Research and Development Program of China under Grant 2021YFB2400500.

* Corresponding author.
E-mail address: gaobingtuan@seu.edu.cn (B. Gao).

https://doi.org/10.1016/j.segan.2022.100955
2352-4677/

proportional to the system frequency deviation in CPFR. Also, the feedback control is adopted in the CPFR so that the control decision is made based on the historical information after the occurrence of the event since it is a corrective control method [15]. Furthermore, due to the inertia of power system, a certain time delay exists in the load power information reflected by the grid frequency. Since the input of the CPFR is the grid frequency deviation, the CPFR could only respond to the grid frequency passively, and the control effects are consequently weakened by the delay to some extent.

With the rapid development of synchronized measurement technologies, such as monitoring system and phasor measurement units (PMUs) in modern power system, sufficient information can be utilized to predict or estimate the states and risks in modern power system [16]. Once the predictive information is taken into consideration, the controller can make control decisions more actively to achieve a better control effect. Hence, the control hysteresis of CPFR can be improved by taking advantage of the predicted states of the power system reasonably.

Meanwhile, a growing number of control techniques are able to take corresponding actions actively according to the predictive information of power system. Model predictive control (MPC), one of the modern control methods, possess two main functions: prediction and optimization. It obtains the optimal control sequence by solving an open loop optimal problem in finite time domain, and only the first control quantity is permitted to be applied to the system. The optimal control sequence will be updated at the next sampling time. Since MPC is skilled in dealing with constrained problems and taking advantage of predictive information, which meets the requirements of the wind power frequency regulation, it is used in the frequency support of wind power in recent years [17–27]. [17] focuses on the wind speed differences among individual wind generators due to the wake effects. [18] and [19] research on the inertial control for wind farms. [20] studies the power dispatch of wind cluster, whose time scale is larger than PFR. A nonlinear MPC with a hierarchical structure is presented in [21] for frequency support of a wind farm, focusing on reducing the computational burden of the central controller. In [22], the Kalman filter is used to estimate the variation in load for MPC to improve wind farm participation to frequency regulation. [23] proposes an inverter-level control strategy based on MPC to ensure the frequency stability, but the mechanical model of the wind turbine is not considered. [24] proposes a load frequency control method based on MPC for the WFs and thermal power plants. However, the constraints of the incremental active power output of WF are not considered properly. Also, the MPC is used to adjust the gain of droop controller of wind turbines while the energy storage system is responsible for the active power required from frequency control [25]. When the turbine operates in MPPT mode, wind speed variations result in active power fluctuations of the WF injecting into power system, and the frequency variation caused by wind speed disturbances is smoothed by using MPC in [26,27].

As introduced in the literature review, impressive achievements have been made in the frequency support of WFs using MPC, while knowledge gaps still exist in the following aspects. (1) There is a lack of analysis of the hysteresis characteristics of the CPFR caused by the governor, high pressure cylinder and other mechanical parts in SGs. (2) Since the output power of CPFR has a peak value corresponding to the frequency nadir, considering the limited reserved power of WFs, proper constraints should be set to achieve frequency support without increasing the rate of power curtailment. (3) The asymptotic stability of MPC applied to frequency support for WFs has not been proved theoretically. (4) The MPC controllers are designed on the basis of MPPT operation mode instead of deloading mode in most studies, and the WFs can only provide temporary frequency support but not the reliable and sustainable PFR which has been clearly required by the national standard in China [28].

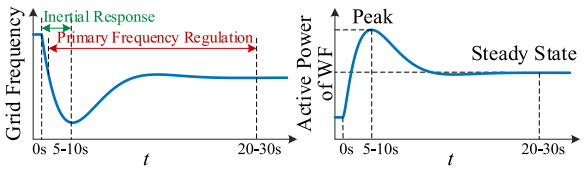

Fig. 1. Schematic diagram of grid frequency and PFR response of WF following a sudden load change.

In this paper, by taking the predictive information into account, we will introduce an active PFR (APFR) strategy for power grid integrated with WFs to enhance control performance of PFR. The main contributions of this paper can be summarized as follows:

1. An APFR strategy based on MPC for grid integrated WFs is proposed, solving the response hysteresis of the CPFR caused by the mechanical parts in SGs and achieving an active, flexible and sustainable PFR without increasing the rate of power curtailment of the WFs.

2. A predictive model is established following the small-signal model of power system integrated with WFs, and the asymptotic stability of the proposed closed-loop control system is proved theoretically though a finite terminal weighting matrix based Lyapunov function.

3. Extensive case studies in standard test systems based on RT-LAB are performed to validate the theoretical analysis and the superiority of the proposed APFR strategy.

The rest of the paper is organized as follows. In Section 2, the characteristics of CPFR are analyzed and the control architecture of APFR for grid integrated WFs is presented. In Section 3, the MPC based APFR controller design procedure is given in detail. Case studies based on RT-LAB are performed and discussed in Section 4. Finally, the conclusions are drawn in Section 5.

2. Overall control architecture

In principle, grid frequency response in 30 s of a power system suffered a sudden disturbance can be divided into two regulation stages in terms of different time scales: inertial response and PFR [29]. As can be seen from Fig. 1 that the response speed of PFR is slower than that of inertial response, caused by the response delay of governor and other mechanical components of the thermal power generator, resulting in the existence of the frequency nadir (FN) at 5–10 s. Owing to the flexibility and rapidity of power electronics devices in the wind power system, the PFR of wind power generators can response as fast as the inertia response. Nevertheless, the power output of CPFR is proportional to the grid frequency deviation, leading to a transient peak of power output of WFs, corresponding to the FN, shown in Fig. 1.

To ensure the WFs can implement PFR for 20 to 30 s, WTs could operate in deloading mode in advance [10,13]. As illustrated in Fig. 1, the peak value of active power output, which has a short duration, is higher than the steady-state value. The reserved power value of WFs should fully consider the peak value of the PFR active power output. Since the peak value of the power output cannot be used in most of the time, CPFR of WFs will lead to an inadequate and unreasonable usage of the reserved power of WFs. Therefore, it is strongly encouraged to solve the problem of how to effectively use the reserved power of WFs within the time scale of PFR.

Thanks to the installations of PMUs, online bus frequency can be measured or estimated, which means the frequency and

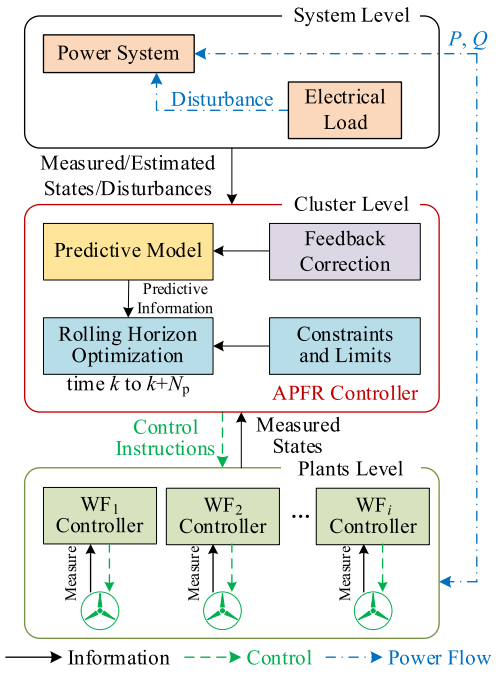

Fig. 2. Overview of the APFR strategy for grid integrated WFs based on MPC.

load power can be treated as a known quantity [18,30]. It is possible for WFs to make corresponding control decisions actively according to the predictive information of power system. Consequently, an APFR strategy for grid integrated WFs based on MPC is proposed, and the control architecture is shown in Fig. 2. The framework of the proposed scheme is divided into 3 layers based on delamination principle from system level to an individual wind farm level in the spatial scale. Measured state variables and disturbances are given by the system level. The APFR controller is implemented in cluster level, responsible for predicting the frequency response characteristics and optimizing the active power reference increments/decrements of WFs for PFR. The control instructions are dispatched to the plants level according to the available incremental and decremental power of each WF, and the WF controller should follow the power command to participate the PFR. Finally, the predictive model will be corrected according to the feedback state variables. By actively predicting or acquiring more system information, the active frequency control is realized.

3. Controller design

Considering the power balance principle, it is noted that the optimal incremental active power of WFs with APFR should equal to the incremental load power, ideally. In this case, WFs should reserve considerable power to participate in PFR, which is uneconomic [31]. Thus, it is necessary to restrict the incremental and decremental power of APFR for WFs. Different from inertial control, PFR will affect the output of wind power in the steady-state. If the APFR strategy generates the active power reference directly based on the ability of active power output of WFs, the steady-state characteristics of WFs will change. As a result, it may produce adverse effects on the researches on power dispatch optimization, system scheduling, frequency stability analysis and power flow calculation, etc. Therefore, the proposed APFR should not only dynamically improve the grid frequency response characteristics, but also be consistent with the CPFR in the steady-state, and an inequality constraint of the

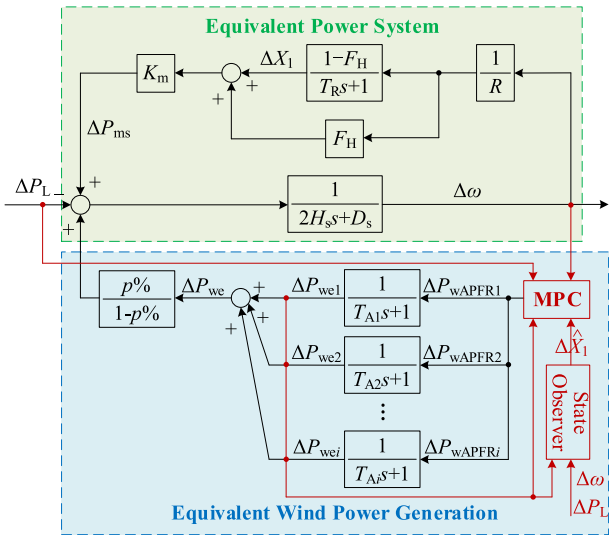

Fig. 3. Small-signal model of power system integrated with WFs based on MPC.

incremental/decremental active power range of APFR should be set according to the predicted power output range of WFs with CPFR in a certain period, which means the predictive model of CPFR should be established to constrain the power output of APFR.

3.1. Predictive model

The system frequency response (SFR) after the disturbance can be predicted based on the low-order SFR model [32]. The predictive model along with the optimization problem can be simplified since the elements with less time coefficient are neglected in the low-order SFR model. Since the electromagnetic transient process of wind power system is much shorter than its electromechanical transient process, electromagnetic regulation process of wind generation and converter can be ignored, and an inertial element is used to represent the wind power generation [33]. In the small-signal model, the single machine equivalent model is used for WFs.

In order to improve the passive performance of CPFR and take reasonable use of the predictive information, MPC is applied in the proposed APFR strategy. The small-signal model of power system integrated with WFs using APFR in per unit (p.u.) based on low-order SFR model is established, shown in Fig. 3.

According to Fig. 3 and inverse Laplace transform theory, the state equations can be expressed as

$$\begin{cases} 2H_s\Delta\dot{\omega} + \dfrac{D_sR - K_mF_H}{R}\Delta\omega = K_m\Delta X_1 + \dfrac{p\%}{1-p\%}\Delta P_{we} - \Delta P_L \\ T_R\Delta\dot{X}_1 + \Delta X_1 = \dfrac{1-F_H}{R}\Delta\omega \\ \Delta P_{we} = \sum_{i=1}^{n_{WF}} \Delta P_{wei} \\ T_{Ai}\Delta\dot{P}_{wei} + \Delta P_{wei} = \Delta P_{wAPFRi},\ \forall i \in N_{WF} \end{cases} \tag{1}$$

where H_s and D_s is the system inertia constant and damping factor, ω is the grid angular frequency, K_m is the mechanical power gain factor, F_H is the fraction of total power generated by the high-pressure turbine, $1/R$ is the PFR gain of the equivalent power system, $p\%$ is the wind power penetration, P_{we} is the sum of the active power output of all WFs, P_L is the load power, T_R is the reheat time constant, X_1 is the output of the low-pressure

turbine in thermal power generator, P_{wei} is the active power output of the WF$_i$, n_{WF} is the number of WFs, T_{Ai} is the equivalent inertia time constant of the WF$_i$, N_{WF} is {1,2,…, n_{WF}}. All variables are per unit value, and the variables with the Δ prefix denotes the incremental value of the corresponding ones.

The state equations in matrix format can be expressed as

$$\begin{cases} \dot{\boldsymbol{x}}_2(t) = \boldsymbol{A}_2\boldsymbol{x}_2(t) + \boldsymbol{B}_2\boldsymbol{u}(t) + \boldsymbol{C}_2 d_2(t) \\ \boldsymbol{y}_2(t) = \boldsymbol{E}_2\boldsymbol{x}_2(t) \end{cases} \tag{2}$$

where $\boldsymbol{x}_2 = [\Delta\omega\ \Delta X_1\ \Delta P_{we1}\ \Delta P_{we2} \ldots \Delta P_{wei}]^{\mathrm{T}}$ is the state vector of the system, $\boldsymbol{u} = [\Delta P_{wAPFR1}\ \Delta P_{wAPFR2}\ \Delta P_{wAPFRi}]^{\mathrm{T}}$ is the input vector of the system, $d_2 = \Delta P_L$ is the disturbance of the system, $\boldsymbol{y}_2 = [\Delta\omega\ 0 \ldots 0]^{\mathrm{T}}$ is the output of the system. It is noted that d_2 is the same as d_1. The purpose of distinguishing d_1 and d_2 is to facilitate reading. Since the ΔX_1 is hard to be measured by WFs, it is estimated by a state observer designed according to the modern control theory, meeting the requirement of convergence rate and the stability of the system. The convergence time is neglected in the predictive model. Then, the ΔX_1 is replaced by $\Delta\hat{X}_1$ in $\boldsymbol{x}_2$.

Matrix $\boldsymbol{A}_2$, $\boldsymbol{B}_2$, $\boldsymbol{C}_2$ and $\boldsymbol{E}_2$ are shown in

$$\boldsymbol{A}_2 = \begin{bmatrix} \frac{K_m F_H - D_s R}{2H_s R} & \frac{K_m}{2H_s} & \frac{p\%}{2H_s(1-p\%)} & \cdots & \frac{p\%}{2H_s(1-p\%)} \\ \frac{1-F_H}{T_R R} & -\frac{1}{T_R} & 0 & \cdots & 0 \\ 0 & 0 & -\frac{1}{T_{A1}} & \cdots & 0 \\ \vdots & \vdots & & \ddots & \\ 0 & 0 & 0 & \cdots & -\frac{1}{T_{Ai}} \end{bmatrix} \tag{3}$$

$$\boldsymbol{B}_2 = \begin{bmatrix} 0 & 0 & \frac{1}{T_{A1}} & \cdots & 0 \\ \vdots & \vdots & & \ddots & \\ 0 & 0 & 0 & \cdots & \frac{1}{T_{Ai}} \end{bmatrix}^{\mathrm{T}} \tag{4}$$

$$\boldsymbol{C}_2 = \begin{bmatrix} -\frac{1}{2H_s} & 0 & 0 & \cdots & 0 \end{bmatrix}^{\mathrm{T}} \tag{5}$$

$$\boldsymbol{E}_2 = \begin{bmatrix} 1 & 0 & 0 & \cdots & 0 \\ 0 & 0 & 0 & \cdots & 0 \\ \vdots & \vdots & \vdots & & \vdots \\ 0 & 0 & 0 & \cdots & 0 \end{bmatrix} \tag{6}$$

According to the MPC theory, taking calculation amount and control effect into consideration, 1/20 times of peak time is selected as the sampling time generally. The discrete form of (2) can be obtained

$$\begin{cases} \boldsymbol{x}_2(k+1) = \boldsymbol{G}_2\boldsymbol{x}_2(k) + \boldsymbol{H}_2\boldsymbol{u}(k) + \boldsymbol{I}_2 d_2(k) \\ \boldsymbol{y}_2(k) = \boldsymbol{E}_2\boldsymbol{x}_2(k) \end{cases} \tag{7}$$

where $\boldsymbol{G}_2 = e^{\boldsymbol{A}_2 t_s}$, $\boldsymbol{H}_2 = \int_0^{t_s} e^{\boldsymbol{A}_2 t_s}\boldsymbol{B}_2 dt$, $\boldsymbol{I}_2 = \int_0^{t_s} e^{\boldsymbol{A}_2 t_s}\boldsymbol{C}_2 dt$, t_s is the sample time. $\boldsymbol{x}_2$, d_2, $\boldsymbol{y}_2$ are the discrete form of the corresponding one in (2). Based on the time step k, the system state variables at time step $k+1$ to $k+N_p$ can be predicted by the predictive model of power system integrated with WFs based on APFR, shown in

$$\begin{cases} \boldsymbol{X}_2(k+N_p) = \boldsymbol{G}_{x2}\boldsymbol{x}_2(k) + \boldsymbol{H}_{x2}\boldsymbol{U}(k) + \boldsymbol{I}_{x2}\boldsymbol{D}_2(k) \\ \boldsymbol{Y}_2(k+N_p) = \boldsymbol{E}_{y2}\boldsymbol{X}_2(k+N_p) \end{cases} \tag{8}$$

where the matrices in (8) are shown from (A.14) to (A.21) in Appendix A.2. On the basis of the same system, the predictive model with CPFR is presented in Appendix A.1.

3.2. Receding horizon optimization

For the receding horizon optimization, linear quadratic regulation (LQR) method is generally utilized in the MPC. The optimization objective is to minimize the frequency deviation in the receding horizon. Meanwhile, the Lyapunov stability of MPC method can be achieved based on the finite terminal weighting matrix [34–36]. The objective function can be defined as

$$\begin{aligned} \min J =\ & \boldsymbol{Y}_2(k+N_p)^T \boldsymbol{Q}_Y \boldsymbol{Y}_2(k+N_p) \\ & + \boldsymbol{U}(k)^T \boldsymbol{R}_U \boldsymbol{U}(k) + \Psi\left[\boldsymbol{x}_2(k+N_p|k)\right] \end{aligned} \tag{9}$$

where $\boldsymbol{Y}_2(k+N_p)$ is the output of the predictive model, $\boldsymbol{U}(k)$ is the input of the predictive model, Q_Y and R_U are the symmetric weighting matrix shown in (A.22)–(A.23), $\Psi[\boldsymbol{x}_2(k+N_p|k)]$ is the finite terminal weighting matrix.

3.2.1. Stability analysis

To evaluate the closed-loop stability of the proposed MPC based APFR control system, we have the following theorem.

Theorem 1. *Suppose that the feedback control law $\boldsymbol{L}(\boldsymbol{x})$, the terminal constraint domain χ and the finite terminal weighting matrix $\Psi(\boldsymbol{x})$ are existing to satisfy the following conditions expressed as equations and inequalities*

$$\begin{cases} 1.\ 0 \in \chi \\ 2.\ \boldsymbol{G}_2\boldsymbol{x} + \boldsymbol{H}_2 L(\boldsymbol{x}) \in \chi, \forall \boldsymbol{x} \in \chi \\ 3.\ \Psi(0) = 0, \Psi \succ 0 \\ 4.\ \Psi(\boldsymbol{G}_2\boldsymbol{x} + \boldsymbol{H}_2 L(\boldsymbol{x})) - \Psi(\boldsymbol{x}) \\ \quad \le -\boldsymbol{x}^T \boldsymbol{E}_2^T \boldsymbol{Q} \boldsymbol{E}_2 \boldsymbol{x} - L(\boldsymbol{x})^T \boldsymbol{R} L(\boldsymbol{x}) \\ 5.\ L(\boldsymbol{x}) \in \boldsymbol{U}, \forall \boldsymbol{x} \in \chi \end{cases} \tag{10}$$

Then, the finite terminal weighting matrix-based MPC stabilizes the system.

Proof. Suppose that the optimal control sequence at the time step k is [$\boldsymbol{u}^*(k|k)$, …, $\boldsymbol{u}^*(k+N-1|k)$], and the corresponding optimal objective function value is $J^*(k)$. According to the Condition 5, the $L(\boldsymbol{x}^*(k+N|k))$ satisfies the input constraint due to $\boldsymbol{x}^*(k+N|k) \in \chi$. It can be obtained based on condition 2 that $\boldsymbol{A}\boldsymbol{x}^*(k+N|k) + \boldsymbol{B}L(\boldsymbol{x}^*(k+N|k)) \in \chi$. Therefore, a feasible solution at time step $k+1$ can be deduced as [$\boldsymbol{u}^*(k+1|k)$, …, $\boldsymbol{u}^*(k+N\text{-}1|k)$, $L(\boldsymbol{x}^*(k+N|k))$]. The objective function at time step $k+1$ can be derived as (A.24), where the variables superscripted with * denote the corresponding optimal one. Based on condition 4 in (10) and (A.24), the inequality that $J^*(k+1) \le J(k+1) \le J^*(k) - \boldsymbol{x}(k)^{\mathrm{T}}\boldsymbol{E}_2{}^{\mathrm{T}}\boldsymbol{Q}\boldsymbol{E}_2\boldsymbol{x}(k) - \boldsymbol{u}(k)^{\mathrm{T}}\boldsymbol{R}_U\boldsymbol{u}(k) = J^*(k) - \boldsymbol{y}(k)^{\mathrm{T}}\boldsymbol{Q}_Y\boldsymbol{y}(k) - \boldsymbol{u}(k)^{\mathrm{T}}\boldsymbol{R}_U\boldsymbol{u}(k)$ can be derived. Therefore, $J^*(k)$ can be selected as a Lyapunov function, ensuring the asymptotic stability of the closed-loop system. Let $L(x) = \boldsymbol{F}\boldsymbol{x}$, $\Psi(\boldsymbol{x}) = \boldsymbol{x}^{\mathrm{T}}\boldsymbol{P}\boldsymbol{x}$ and $\chi = \{\boldsymbol{x} | \boldsymbol{x}^{\mathrm{T}}\boldsymbol{P}\boldsymbol{x} \le r\}$, where $\boldsymbol{P} = \boldsymbol{P}^{\mathrm{T}} > 0$. Under these circumstances, Condition 2 is implied in Condition 4 which can be expressed as follows

$$(\boldsymbol{G}_2 + \boldsymbol{H}_2\boldsymbol{F})^{\mathrm{T}}\boldsymbol{P}(\boldsymbol{G}_2 + \boldsymbol{H}_2\boldsymbol{F}) - \boldsymbol{P} \le -\boldsymbol{E}_2^{\mathrm{T}}\boldsymbol{Q}\boldsymbol{E}_2 - \boldsymbol{F}^{\mathrm{T}}\boldsymbol{R}\boldsymbol{F} \tag{11}$$

Let $\boldsymbol{P} = r\boldsymbol{S}^{-1}$ and $\boldsymbol{Y} = \boldsymbol{F}\boldsymbol{S}$. According to the Schur complement theorem, Eq. (11) can be transformed into the following linear matrix inequality (LMI).

$$\begin{bmatrix} \boldsymbol{S} & \boldsymbol{S}\boldsymbol{G}_2^T + \boldsymbol{Y}^T\boldsymbol{H}_2^T & \boldsymbol{S}\boldsymbol{E}_2^T\boldsymbol{Q}^{1/2} & \boldsymbol{Y}^T\boldsymbol{R}^{1/2} \\ \boldsymbol{G}_2\boldsymbol{S} + \boldsymbol{H}_2\boldsymbol{Y} & \boldsymbol{S} & 0 & 0 \\ \boldsymbol{Q}^{1/2}\boldsymbol{E}_2\boldsymbol{S} & 0 & r\boldsymbol{I} & 0 \\ \boldsymbol{R}^{1/2}\boldsymbol{Y} & 0 & 0 & r\boldsymbol{I} \end{bmatrix} \ge 0 \tag{12}$$

If the input constraint is expressed as $U = \{u| -u_{\max} \le u \le u_{\max}\}$, the Condition 5 can be transformed into the following LMI.

$$\begin{cases} \begin{bmatrix} \boldsymbol{Z} & \boldsymbol{Y} \\ \boldsymbol{Y}^T & \boldsymbol{S} \end{bmatrix} \ge 0 \\ \boldsymbol{Z}_{jj} \le u_{j.\max}^2, \quad j = 1, 2, \ldots, N_p \end{cases} \tag{13}$$

If r, $\boldsymbol{Y}$, $\boldsymbol{S}$, $\boldsymbol{Z}$ satisfy (12) and (13), the MPC method based on finite terminal weighting matrix can promise the asymptotic stability of the closed-loop system. The theorem is proved. The $\Psi[\boldsymbol{x}_2(k+N_p|k)]$ is substituted by $\boldsymbol{x}_2^T(k+N_p|k)\boldsymbol{P}\boldsymbol{x}_2(k+N_p|k)$.

3.2.2. Objective function standardization

For the convenient expression, $\boldsymbol{X}_2$ represents $\boldsymbol{X}_2(k+N_p)$, $\boldsymbol{x}_2$ represents $\boldsymbol{x}_2(k)$, $\boldsymbol{U}$ represents $\boldsymbol{U}(k)$, and $\boldsymbol{D}_2$ represents $\boldsymbol{D}_2(k)$ in this subsection. The objective function (9) can be written as

$$\begin{aligned} \min J\left(k+N_p\middle|k\right) &= \boldsymbol{X}_2^T\boldsymbol{E}_{y2}^T\boldsymbol{Q}_Y\boldsymbol{E}_{y2}\boldsymbol{X}_2 + \boldsymbol{U}^T\boldsymbol{R}_U\boldsymbol{U} \\ &\quad + \boldsymbol{x}_2^T\left(k+N_p\middle|k\right)\boldsymbol{P}\boldsymbol{x}_2\left(k+N_p\middle|k\right) \end{aligned} \tag{14}$$

Let $\boldsymbol{x}_2(k+N_p|k) = \boldsymbol{V}_x\boldsymbol{W}$, $\boldsymbol{W} = \boldsymbol{G}_{x2}\boldsymbol{x}_2 + \boldsymbol{H}_{x2}\boldsymbol{U} + \boldsymbol{I}_2\boldsymbol{D}_2$, $\boldsymbol{V} = \boldsymbol{E}_{y2}^T\boldsymbol{Q}_Y\boldsymbol{E}_{y2} + \boldsymbol{V}_x^T\boldsymbol{P}\boldsymbol{V}_x$. Then, according to (8) and (14), the standard form of the quadratic optimization objective function can be deduced as

$$\begin{aligned} &\min J\left(k+N_p\middle|k\right) \\ &= \min\left(\boldsymbol{W}^T\boldsymbol{E}_{y2}^T\boldsymbol{Q}_Y\boldsymbol{E}_{y2}\boldsymbol{W} + \boldsymbol{W}^T\boldsymbol{V}_x^T\boldsymbol{P}\boldsymbol{V}_x\boldsymbol{W} + \boldsymbol{U}^T\boldsymbol{R}_U\boldsymbol{U}\right) \\ &= \min\left(\boldsymbol{U}^T\boldsymbol{H}_{x2}^T\boldsymbol{V}\boldsymbol{H}_{x2}\boldsymbol{U} + \boldsymbol{U}^T\boldsymbol{R}_U\boldsymbol{U} + \boldsymbol{x}_2^T\boldsymbol{G}_{x2}^T\boldsymbol{V}\boldsymbol{H}_{x2}\boldsymbol{U}\right. \\ &\quad + \boldsymbol{U}^T\boldsymbol{H}_{x2}^T\boldsymbol{V}\boldsymbol{G}_{x2}\boldsymbol{x}_2 + \boldsymbol{D}_2^T\boldsymbol{I}_2^T\boldsymbol{V}\boldsymbol{H}_{x2}\boldsymbol{U} \\ &\quad \left.+ \boldsymbol{U}^T\boldsymbol{H}_{x2}^T\boldsymbol{V}\boldsymbol{I}_2\boldsymbol{D}_2 + \text{Constant term}\right) \end{aligned} \tag{15}$$

where $\boldsymbol{U}$ is the optimization objective. The term irrelevant to $\boldsymbol{U}$ can be regarded as a constant term and neglected. It can be derived that the quadratic item of the objective function is $\boldsymbol{H}_{x2}^T\boldsymbol{V}\boldsymbol{H}_{x2} + \boldsymbol{R}_U$, and the first order item is $2(\boldsymbol{x}_2^T\boldsymbol{G}_{x2}^T\boldsymbol{V}\boldsymbol{H}_{x2} + \boldsymbol{D}_2^T\boldsymbol{I}_2^T\boldsymbol{V}\boldsymbol{H}_{x2})$.

3.2.3. Constraints

The constraints are presented as follows.

(1) Power ramping rate constraints

$$-P_{wri,\max} \le \Delta P_{wAPFRi}(k+i+1) - \Delta P_{wAPFRi}(k+i) \le P_{wri,\max} \quad \forall i \in N_{WF} \tag{16}$$

where $P_{wri,\max}$ is the upper bound of the ramping rate of the WF$_i$ active power output.

(2) Available incremental PFR power constraints

$$\Delta P_{wAPFRi,\min} \le \Delta P_{wAPFRi} \le \Delta P_{wAPFRi,\max} \qquad \forall i \in N_{WF} \tag{17}$$

where $\Delta P_{wAPFRi,\max}$ and $\Delta P_{wAPFRi,\min}$ are the maximum and minimum incremental power of WF$_i$ with CPFR in the receding period respectively.

As discussed in Section 2, CPFR cannot take full advantage of the reserved power since its input variable is the current system frequency. Therefore, both of the past and predictive information are used in APFR to guarantee the superiority of the control decision and ensure the maximum output power do not exceed the CPFR at the same time. The predictive information of WF$_i$ is contained in (A.7), and the past information can be recorded in the controller as follows

$$\boldsymbol{P}_{wpasti} = \begin{bmatrix} \Delta P_{wCPFRi}\left(k-N_{past}+1\right) \\ \Delta P_{wCPFRi}\left(k-N_{past}+2\right) \\ \vdots \\ \Delta P_{wCPFRi}(k) \end{bmatrix} \tag{18}$$

where N_{past} is the step number of the past information. According to (A.7) and (18), the $\Delta P_{wPFRi,\max}$ and $\Delta P_{wAPFRi,\min}$ can be derived

$$\Delta P_{wAPFRi,\max} = \max\begin{bmatrix} \boldsymbol{P}_{wpasti} \\ \boldsymbol{P}_{wCPFRi} \end{bmatrix} \tag{19}$$

$$\Delta P_{wAPFRi,\min} = \min\begin{bmatrix} \boldsymbol{P}_{wpasti} \\ \boldsymbol{P}_{wCPFRi} \end{bmatrix} \tag{20}$$

(3) Power dispatch constraints

$$\Delta P_{wAPFR,i} = \alpha_i \sum_{j=1}^{n_{WF}} \Delta P_{wAPFR,j}, \qquad \forall i \in N_{WF} \tag{21}$$

The power dispatch ratio α_i is introduced to dispatch the PFR power of WFs, shown in

$$\alpha_i = \frac{P_{wava,i}}{\sum_{j=1}^{n_{WF}} P_{wava,j}}, \forall i \in N_{WF} \tag{22}$$

For the ith WF, its available incremental/decremental power can be obtained [18]

$$P_{wava,i} = \begin{cases} P_{wmax,i} - P_{we,i}, & \Delta P_{wAPFR,i} \ge 0 \\ P_{we,i} - P_{wmin,i}, & \Delta P_{wAPFR,i} < 0 \end{cases} \tag{23}$$

where $P_{wava,i}$ is the available incremental/decremental active power of the WF$_i$, $P_{wmax,i}$ and $P_{wmin,i}$ is the maximum and minimum active power output of the WF$_i$, $P_{we,i}$ is the active power output of the WF$_i$. It is noted that since the PFR is a continuous support process, WFs should operate on the right side of the MPPT curve with the deloading mode. The dispatch method considering stored kinetic energy is generally used for temporary inertia support, while the dispatch based on active power margin is more suitable for APFR. Besides, the WF is described by a single machine equivalent model, without considering the active power distribution in the WF.

3.3. Feedback correction

In order to deal with the inaccuracy of the predictive model, the feedback correction is adopted by MPC. The parameter of the predictive model can be modified by the parameter estimation using Levenberg–Marquardt method every 5 min to ensure the accuracy of the predictive model of CPFR and APFR in 3.1. Specifically, parameters in matrices $\boldsymbol{A}_1$, $\boldsymbol{B}_1$, $\boldsymbol{C}_1$, $\boldsymbol{A}_2$, $\boldsymbol{B}_2$, $\boldsymbol{C}_2$ can be corrected according to the measured/estimated data during the last period. Correspondingly, the discrete forms and the predictive model of MPC are modified.

3.4. Control limit

If the deloading control is adopted, it allows the active power output to exceed the MPPT power for a short time due to the kinetic energy stored in the turbine and drivetrains. Besides, the small-signal stability of WT is jeopardized if it operates on the left side of the maximum power point [37]. In order to achieve the stable operation of wind turbine when overloading, the upper

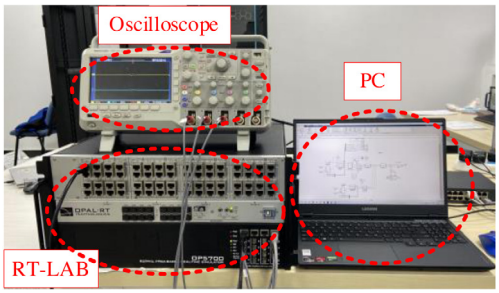

Fig. 4. RT-LAB platform.

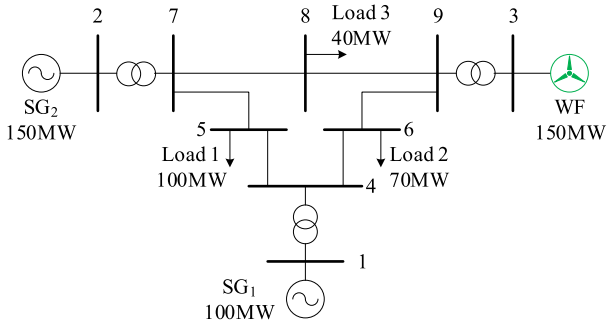

Fig. 5. 3-machine 9-bus power system with a WF integrated at bus 3.

limit of the APFR power variation of WF$_i$ can be expressed as follows [38]

$$\Delta P_{\mathrm{wAPFR}i,\mathrm{ul}} = P_{wi}^{\mathrm{MPPT}} - P_{\mathrm{wei}} \qquad \forall i \in N_{\mathrm{WF}} \tag{24}$$

$$P_{wi}^{\mathrm{MPPT}} = \min\left(\frac{\rho\pi R_{\mathrm{w}}^5 C_{\mathrm{Pmax}}}{2\lambda_{\mathrm{opt}}^3}\omega_{\mathrm{w}}^3, P_{\mathrm{nw}i}\right) \forall i \in N_{\mathrm{WF}} \tag{25}$$

where $\Delta P_{\mathrm{wAPFR}i,\mathrm{ul}}$ is the upper limit of the APFR power variation of the ith WF, PMPPT wi is the active power of the ith WF with MPPT, $P_{\mathrm{nw}i}$ is the rated power of the ith WF, ρ, R_{w}, C_{Pmax}, and λ_{opt} are the air density, rotor radius, maximum power coefficient, and optimal tip-speed ratio, respectively.

Meanwhile, the lower limit of the output power of WF is specified by the national standard in China. The WF should participate in PFR if its output active power of WF is larger than 0.2 p.u. The lower limit of the APFR power variation of WF$_i$ is obtained

$$\Delta P_{\mathrm{wAPFR}i,\mathrm{ll}} = P_{\mathrm{wei}} - 0.2 \qquad \forall i \in N_{\mathrm{WF}} \tag{26}$$

where $\Delta P_{\mathrm{wAPFR}i,\mathrm{ll}}$ is the lower limit of the APFR power variation of WF$_i$. Then, the available incremental PFR power constraints should be modified as

$$\Delta P_{\mathrm{wAPFR}i,\mathrm{ll}} \le \Delta P_{\mathrm{wAPFR}i} \le \Delta P_{\mathrm{wAPFR}i,\mathrm{ul}} \qquad \forall i \in N_{\mathrm{WF}} \tag{27}$$

Thus far, the controller design is completed. Compared with CPFR, the APFR can take active measures to deal with (1) the response hysteresis of the mechanical parts in SGs, (2) the hysteresis characteristics of frequency caused by the power system inertia. Meanwhile, constraints are set to restrict the feasible region, ensuring the control stability and security.

Besides, the wind speed is regarded as a constant value in the receding horizon of MPC, since the wind speed variation is hard to be predicted within the time scale of PFR, and the influence of wind speed can be updated each time a sample is taken, reducing the impact of the wind speed variation on the control effect.

4. Case study

To verify the validity of the theoretical analysis and the effectiveness of the proposed APFR scheme, case studies of 3-machine 9-bus system, 4-machine 2-area system and 10-machine 39-bus based on RT-LAB OP5700 are carried out, as shown in Fig. 4. The oscilloscope connected to RT-LAB is used to directly observe the output data with accurate timestamp during the simulation.

4.1. WSCC 3-machine 9-bus system

The WSCC 3-machine 9-bus system integrated with a WF is established [39,40], shown in Fig. 5. The adopted parameters of SGs and the WF are listed in Table 1. The stability of the system with different F_{H} is analyzed in Appendix A.3.

Table 1
Parameters of 3-machine 9-bus system.

SG parameters	Values	WF parameters	Values
H_{s}, s	7	T_{A}, s	0.2
D_{s}	1	K_{wP}	−20
K_{m}	0.95	p%	37.5%
F_{H}	0.3	t_{s}, s	0.2
R	−0.05	N_{p}	50
T_{R}	8	N_{past}	25

It should be mentioned that the frequency nadir always comes at 5–10 s after the disturbance occurs. The time can be further shortened with the wind power penetration increasing, and it is the most important index of APFR. Since the matrix dimension in the predictive model is determined by the value of N_{p}, the N_{p} is chosen as 50 to keep a balance between the computational burden and the control effect, and the prediction horizon is 10 s to make sure the frequency nadir is contained. The wind speed of the WF is 9 m/s.

4.1.1. Load increasing

To test the performance of APFR, the scenario of load increasing is imitated. The load power of load 3 at bus 8 has a 0.06 p.u. step change at $t = 1$ s. The grid frequency, power reference of PFR, equivalent angular speed and equivalent pitch angle of the WF are shown in Fig. 6.

In Fig. 6(a), the grid frequency nadir with CPFR strategy occurs when $t = 3.2$ s which is 49.853 Hz, while the grid frequency with APFR drops to the nadir of 49.867 Hz at $t = 4.2$ s. It can be obtained that the proposed APFR raises the peak time of the grid frequency by 1 s and the frequency nadir is increased by 9.5%. As illustrated in Fig. 6(b), the maximum power output of the CPFR can be predicted by the APFR. Once the load power disturbance is detected, the P_{wAPFR} is increased by 0.059 p.u. according to the results of the receding horizon optimization. The P_{wAPFR} declines gradually after the CPFR achieve the maximum reference value. The main difference between CPFR and APFR is that the APFR can make active control decision in advance according to the predictive information. The prediction horizon is 10 s, and the frequency nadir can be predicted by APFR strategy. The peak value of active power reference can be calculated to make the WF act in advance. It can be found that the APFR can make control decision according to the peak value of the power of CPFR, and the maximum value of P_{wAPFR} is equal to that of P_{wCPFR}. Therefore, the APFR can response faster than CPFR. In this case, the APFR can achieve better dynamic control effect by predicting the frequency nadir in advance, optimizing in the finite time domain and utilizing the power capacity of PFR reasonably. Besides, after the peak power of CPFR occurring, the P_{wAPFR} will remain that value for 5s more due to the utilization of the past information, and then drop to the steady state smoothly. Because the wind power operates in the deloading mode, the wind energy captured by the

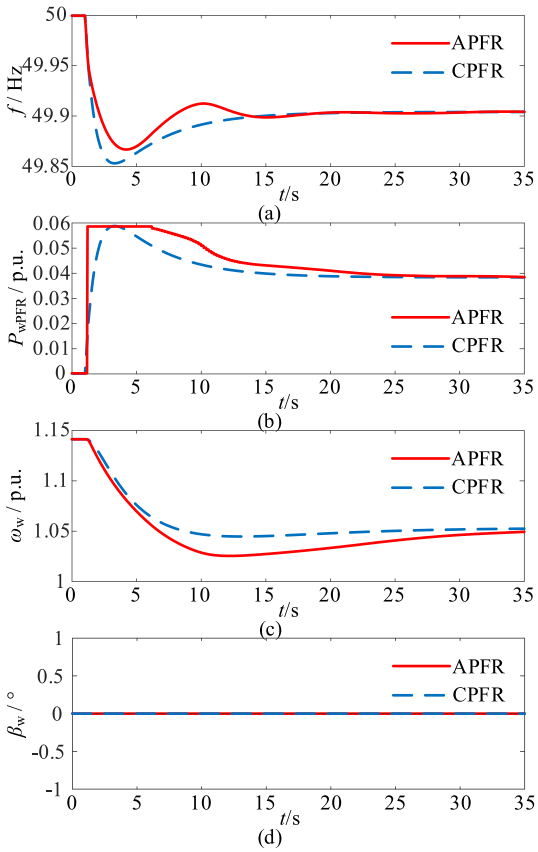

Fig. 6. Waveform of (a) grid frequency, (b) power reference of PFR, (c) equivalent rotor speed of the WF, (d) equivalent pitch angle of the WF with different control strategies when load increases.

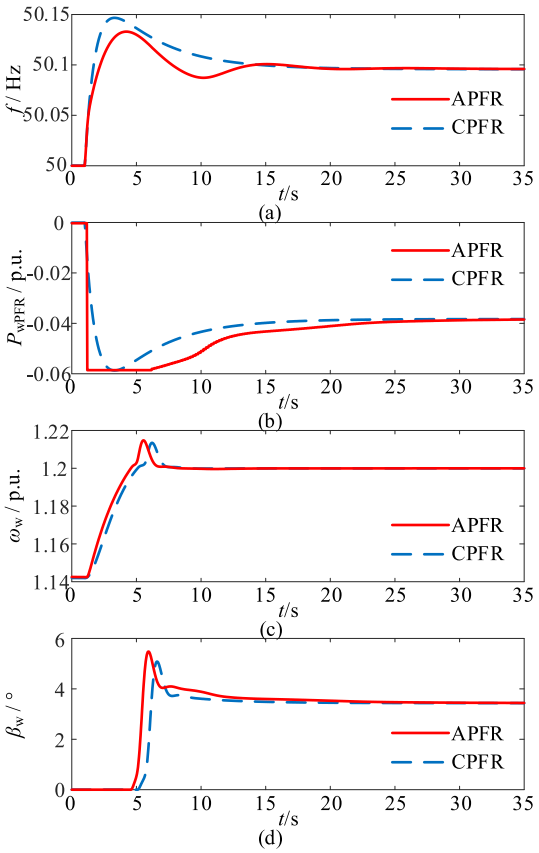

Fig. 7. Waveform of (a) grid frequency, (b) power reference of PFR, (c) equivalent rotor speed of the WF, (d) equivalent pitch angle of the WF with different control strategies when load decreases.

WF can be increased by reducing the rotor speed [3] to reach the electric power balance, shown in Fig. 6(c). Since the equivalent rotor speed do not reach 1.2 p.u. which is the upper limit, the pitch angle remains unchanged based on the pitch angle control strategy, shown in Fig. 6(d). Therefore, compared to the CPFR, the dynamic characteristics of the grid frequency can be improved by APFR without increasing the curtailed power of the WF.

4.1.2. Load decreasing

In this scenario, the load power of load 3 at bus 8 has a −0.06 p.u. step change at $t = 1$ s. The grid frequency, power reference of PFR, equivalent angular speed and equivalent pitch angle of the WF are shown in Fig. 7.

As can be seen in Fig. 7(a), the peak of grid frequency with CPFR strategy, which is 50.147 Hz, occurs when $t = 3.3$ s, while the grid frequency with APFR rises to the nadir of 50.133 Hz at $t = 4.2$ s. As the load fluctuation is opposite to that in load increasing scenario in Section 4.1.1, the optimization results in Figs. 7(b) and Fig. 6(b) are also opposite to each other. Additionally, owing to the decreasing load power, the WF should increase the rotor speed to reduce the captured wind energy. After the rotor speed reaches 1.2 p.u., the pitch angle starts to move. Since the pitch angle change will cause mechanical wear and maximum change speed of pitch angle is 10°/s, the rotor speed will exceed 1.2 p.u. for about 1.5 s. After the pitch angle changes to a certain degree, the rotor speed keeps stable at 1.2 p.u.

4.1.3. Load continuous changing

In this scenario, the load power of load 3 at bus 8 has a 0.05 p.u. step change at $t = 1$ s and then has a −0.05 p.u. step change when $t = 3$ s. The grid frequency, power reference of PFR and equivalent angular speed of the WF are shown in Fig. 8.

As shown in Fig. 8, the maximum power reference of CPFR can be predicted by the APFR accurately after the load increasing at $t = 1$ s, and the P_{wAPFR} is adjusted to 0.049 p.u. directly once the disturbance is found. The grid frequency drops to the nadir when $t = 5$ s, and the P_{wCPFR} reaches 0.049 p.u., which is the peak value, demonstrating the frequency prediction accuracy of the MPC. Besides, the frequency nadirs of the CPFR and APFR are 49.878 Hz and 49.904 Hz respectively, improved by 21.3%. After the disturbance disappears, the grid frequency begins to recover. In Fig. 8(a), the frequency overshoot of APFR is less than that of CPFR at about $t = 7$ s, and the grid frequency with APFR returns to the nominal value when $t = 11$ s while the grid frequency reaches the steady-state at $t = 15$ s. In summary, the proposed APFR strategy can deal with the continuous change of load power effectively. The APFR based on MPC optimizes the control quantity P_{wAPFR} in each time step to ensure the grid frequency achieves the steady-state value smoothly and quickly, improving the dynamic characteristics of the grid frequency.

4.2. 4-Machine 2-area system

To further demonstrate the performance of the proposed strategy, a 4-machine 2-area system [29,41] is built. Three WFs are integrated into the system, shown in Fig. 9. The load power, grid frequency, power reference of PFR and active power of the WFs are shown in Fig. 10. The system parameters are listed in Table 2. The wind speeds of WF_1 to WF_3 are set to 10 m/s, 9 m/s and 8 m/s, respectively.

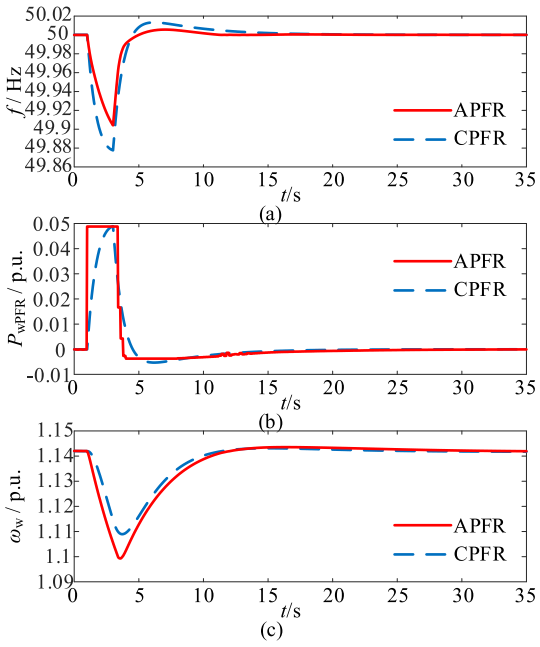

Fig. 8. Waveform of (a) grid frequency, (b) power reference of PFR, (c) equivalent rotor speed of the WF with different control strategies when load continuous changes.

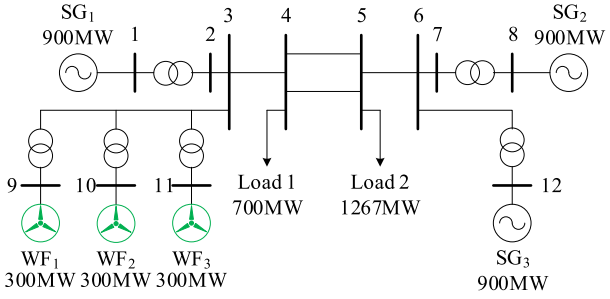

Fig. 9. 4-machine 2-area power system with 3 WFs integrated at bus 3.

Table 2
Parameters of 4-machine 2-area system.

SG parameters	Values	WF parameters	Values
H_s, s	7	T_A, s	0.2
D_s	1	p%	25%

Fig. 10(a) shows the power variation of Load 1 at bus 4. It can be obtained from Fig. 10(b) that the grid frequency deviation is smaller with APFR strategy. The grid frequency reaches the nadir at $t = 4$ s and achieves the peak value when $t = 11.2$ s. Compared to CPFR strategy, the APFR improves the frequency nadir and peak value by 29.81% and 8.57%.

When $t = 2$ s, the minimum frequency in the next 20 s is predicted by MPC. The load power starts to decrease when the frequency does not reach the theoretical minimum value, shown in Fig. 10(a) and (b), which means the system frequency will not drop to the theoretical minimum value. Since the CPFR takes the grid frequency as the input, the P_{wCPFR} cannot reach the maximum value after the load disturbance weakened. Therefore, compared with the load increasing scenario in Section 4.1.1, the

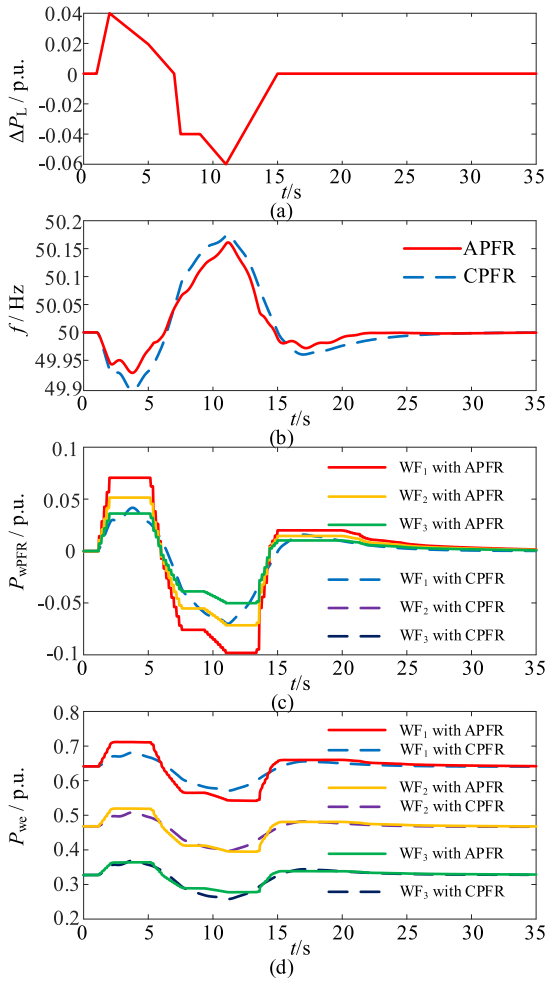

Fig. 10. Waveform of (a) load power variation, (b) grid frequency, (c) power reference of PFR, (d) active power output of the WFs with different control strategies when load fluctuates randomly.

effect of APFR is better in this scenario. In Fig. 10(c), the P_{wCPFR} of WF_1 to WF_3 with CPFR are the same due to the equal PFR proportion coefficient K_{wP}. In contrast, the total active power demand is dispatched according to the available incremental and decremental power of WFs by the MPC in APFR. The WF1 has the strongest ability to implement PFR owing to the highest wind speed. Thus, the active power variation of WF_1 with APFR is larger than that with CPFR, and the active power variation of WF_3 with APFR is smaller than that with CPFR, which means that the PFR involvement level of each WF is corresponding to the reserved active power. As a consequence, the above analysis indicates that the proposed APFR can effectively handle the slope disturbance which is closer to the real power system load fluctuation. Meanwhile, each WF can be coordinated to participate in the PFR based on its own active power reserve.

4.3. New England 39-bus system

To demonstrate the advantage of the APFR strategy over other MPC strategy, the New England 39-bus system is established. Four WFs are integrated into the system, shown in Fig. 11. The penetration of WFs is 24.2%.

The inertia control scheme in [18] is applied, called MPC-based stepwise inertia control (MPC-SIC). In this scenario, the load power at bus 9 has a −0.054 p.u. step change at $t = 5$ s.

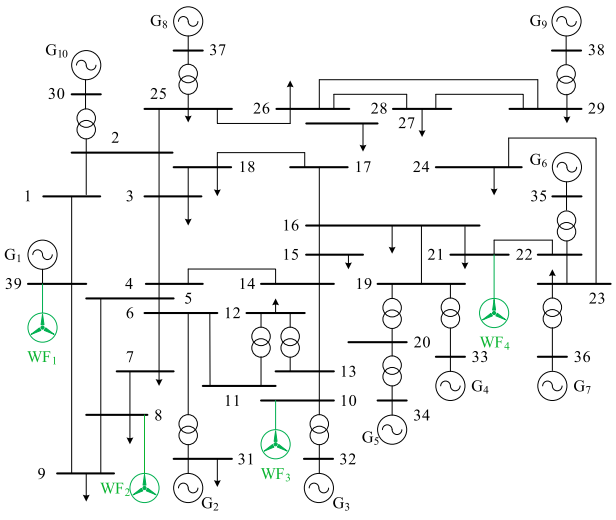

Fig. 11. New England 39-bus system with 4 integrated WFs.

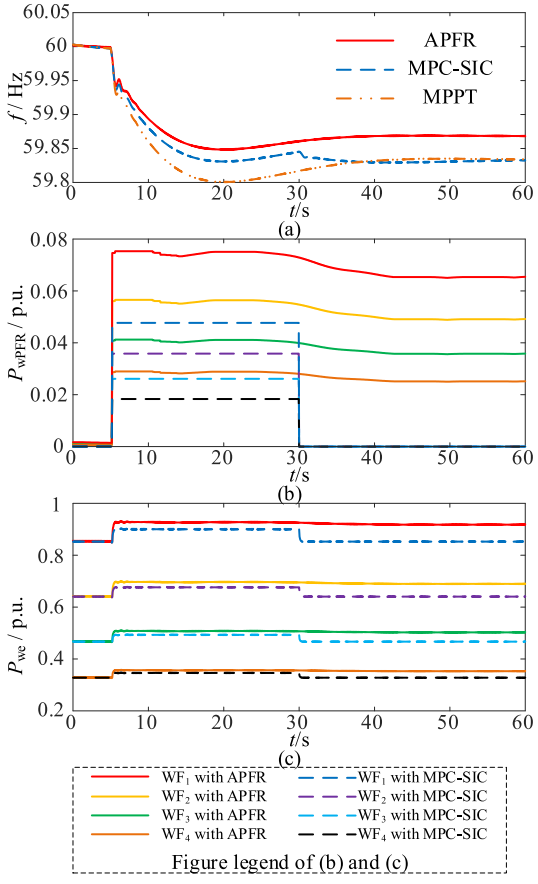

Fig. 12. Waveform of (a) grid frequency, (b) power reference of PFR, (c) active power output of the WFs with different control strategies.

The grid frequency, power reference of PFR and active power of the WFs are shown in Fig. 12. The wind speeds of WF1 to WF4 are set to 11 m/s, 10 m/s, 9 m/s and 8 m/s, respectively.

Fig. 12(a) shows the frequency variation of the system. It can be seen that the grid frequency deviation of the system with APFR is the smallest one. Since the MPC-SIC is an improvement of the SIC, it is required that the support power of WFs should be drop to zero after withdrawing from the temporary

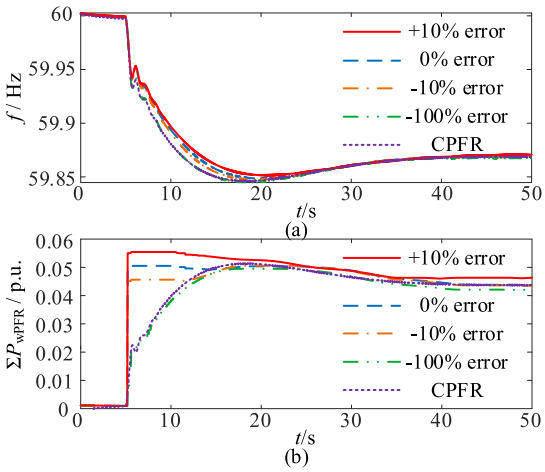

Fig. 13. Waveform of (a) grid frequency, (b) sum of the power references of PFR of WFs.

frequency regulation. As it withdraws the frequency regulation using a stepwise approach, the power fluctuations of WFs will have an impact on the system frequency, resulting in a secondary frequency drop (SFD). The higher the initially support power of MPC-SIC, the deeper the SFD when withdrawing from frequency regulation. Therefore, in order to improve the SFD, the support power at its beginning stage should not be too large, which is the main reason which restricts the frequency support effect of MPC-SIC. Nevertheless, the proposed APFR is an improvement of the sustained PFR. Since the WFs operate in deloading mode in advance, it can provide reliable incremental active power within the PFR time scale. Comparing the three systems in Sections 4.1–4.3, the 39-bus system has the largest number of SGs, the largest equivalent inertia, and the longest time for the frequency to reach the nadir. It can be seen that WFs with the proposed strategy are effective in providing frequency support in different systems.

For the WF cluster, the centralized controller and the communication device among WFs are required to be equipped in the cluster layer. The software algorithm can be updated in the cluster centralized controller. Alternatively, the proposed controller can be applied to the WF controller. No additional hardware cost is required. The strategy proposed in this paper adopts the linear optimization and finally standardized to LQR model, which requires much lower computational efficiency of the controller than nonlinear optimization. The optimization problem can be solved within 0.0215 s on a personal computer with an AMD Ryzen 7 4800H CPU.

4.4. Robustness to load disturbance

In order to further demonstrate the robustness of the proposed strategy to load disturbance, several error bounds of load disturbance estimation are selected for the test in New England 39-bus system. The load disturbance scenario is the same as that in Section 4.3. Deviations of +10%, −10% and −100% (no load disturbance detected) of the estimated value of the load disturbance in APFR are set. The frequency response characteristics of the system and the variation of the total active power reference of the WFs are shown in Fig. 13.

As can be seen in Fig. 13, if the load estimation deviates by +10%, the APFR will provide more aggressive frequency support. If the load estimation deviation is negative, it will provide weaker frequency support. When the deviation of the load estimate is −100%, by which means the input load disturbance of MPC is 0 while the frequency event occurs, APFR still provides

similar frequency support as CPFR. Therefore, the improvement effect of the proposed strategy on the CPFR is influenced by the load estimation/measurement capability. In the event of bounded noise disturbance in the load estimation/measurement, APFR still performs the frequency support task. The lower the load estimated/measured value is than the real value, the weaker the improvement of CPFR, but the worst effect is similar as CPFR. If the load estimated/measured value is larger than the real value, the frequency support effect will be more significant. Since the support power is constrained by the active power margin, it will not jeopardize the operational safety of WFs even if the load estimated/measured value is much larger than the real one.

5. Conclusion

This paper proposes an APFR strategy for grid integrated WFs based on MPC to achieve an active and flexible frequency support. The predictive model of CPFR and APFR are established to constrain the optimal feasible region and determine the objective function of receding horizon optimization, respectively. The asymptotic stability of the proposed controller is verified based on the Lyapunov function theoretically.

Case studies with 3-machine 9-bus system, 4-machine 2area system and 10-machine 39-bus system were performed and analyzed extensively, and the results show that the proposed APFR strategy can predict the grid frequency dynamics and improve the dynamic characteristics of the grid frequency. Besides, the APFR has a satisfying performance in dealing with the continuous load power disturbance and coordinating the reasonable operation of multiple WFs. The improvement effect of the frequency nadir/peak can reach up to 29.81% in the studied scenarios.

Moreover, APFR requires the same power reserve as CPFR, and the power output of WFs with APFR is equal to that with CPFR in the steady-state. Hence, researches on power dispatch optimization, PFR proportion coefficient variation, frequency stability analysis and power flow calculation are still applicable to the controller proposed in the paper. However, the wake effect among WTs in one WF is not taken into consideration. The research on the optimization of WTs' operation point in the steady-state considering wake effect and the corresponding power sharing issue in a WF will be investigated in our future work.

CRediT authorship contribution statement

Zhengyang Hu: Conceptualization, Methodology, Software, Formal analysis, Writing – original draft, Writing – review & editing. **Bingtuan Gao:** Conceptualization, Supervision, Writing – review & editing. **Ruizhe Sun:** Validation, Investigation.

Declaration of competing interest

The authors declare that they have no known competing financial interests or personal relationships that could have appeared to influence the work reported in this paper.

Data availability

No data was used for the research described in the article.

Appendix

A.1. Predictive model of CPFR

The small-signal model of power system integrated with WFs using CPFR in per unit (p.u.) based on low-order SFR model is established, referring to Fig. 3 and replacing MPC with a proportional control of system frequency. The state equations in matrix format can be expressed as

$$\begin{cases} \dot{\boldsymbol{x}}_1(t) = \boldsymbol{A}_1\boldsymbol{x}_1(t) + \boldsymbol{B}_1 d_1(t) \\ y_1(t) = \boldsymbol{C}_1\boldsymbol{x}_1(t) \end{cases} \tag{A.1}$$

where $\boldsymbol{x}_1 = [\Delta\omega\ \Delta X_1\ \Delta P_{we1}\ \Delta P_{we2}\ \Delta P_{wei}]^T$ is the state vector of the system, $d_1 = \Delta P_L$ is the disturbance of the system, $y_1 = \Delta\omega$ is the output of the system. It should be noted that this is not the only way to select the state variables. Different selections of state variables will not influence the output of the system but will change the form of state-space equation. The control variables of CPFR are proportional to $\Delta\omega$ and implicit in (A.1).

Matrix $\boldsymbol{A}_1$, $\boldsymbol{B}_1$ and $\boldsymbol{C}_1$ are shown in

$$\boldsymbol{A}_1 = \begin{bmatrix} \frac{K_m F_H - D_s R}{2H_s R} & \frac{K_m}{2H_s} & \frac{p\%}{2H_s(1-p\%)} & \cdots & \frac{p\%}{2H_s(1-p\%)} \\ \frac{1-F_H}{T_R R} & -\frac{1}{T_R} & 0 & \cdots & 0 \\ \frac{K_{wP1}}{T_{A1}} & 0 & -\frac{1}{T_{A1}} & \cdots & 0 \\ \vdots & \vdots & & \ddots & \\ \frac{K_{wPi}}{T_{Ai}} & 0 & 0 & \cdots & -\frac{1}{T_{Ai}} \end{bmatrix} \tag{A.2}$$

$$\boldsymbol{B}_1 = \begin{bmatrix} -\frac{1}{2H_s} & 0 & 0 & \cdots & 0 \end{bmatrix}^T \tag{A.3}$$

$$\boldsymbol{C}_1 = \begin{bmatrix} 1 & 0 & 0 & \cdots & 0 \end{bmatrix} \tag{A.4}$$

where K_{wPi} is the PFR gain of the WF_i. Discrete state-space equation can be obtained by discretizing (A.1).

$$\begin{cases} \boldsymbol{x}_1(k+1) = \boldsymbol{G}_1\boldsymbol{x}_1(k) + \boldsymbol{H}_1 d_1(k) \\ y_1(k) = \boldsymbol{C}_1\boldsymbol{x}_1(k) \end{cases} \tag{A.5}$$

where $\boldsymbol{G}_1 = e^{\boldsymbol{A}_1 t_s}$, $\boldsymbol{H}_1 = \int_0^{t_s} e^{\boldsymbol{A}_1 t_s}\boldsymbol{B}_1 dt$, $\boldsymbol{x}_1$, d_1, $\boldsymbol{y}_1$ are the discrete form of the corresponding one in (A.1).

Based on the time step k, the system state variables at time step $k+1$ to $k+N_p$ can be predicted by the predictive model of power system integrated with WFs using CPFR shown in

$$\begin{cases} \boldsymbol{X}_1(k+N_p) = \boldsymbol{G}_{x1}\boldsymbol{x}_1(k) + \boldsymbol{H}_{x1}\boldsymbol{D}_1(k) \\ \boldsymbol{Y}_1(k+N_p) = \boldsymbol{C}_{y1}\boldsymbol{X}_1(k+N_p) \end{cases} \tag{A.6}$$

where the matrices in (A.6) are shown from (A.8) to (A.13) in the Appendix, and the N_p is the number of prediction horizon point.

According to (A.6), the corresponding incremental active power of WF_i with CPFR from time k to $k+N_p$ can be obtained as

$$\boldsymbol{P}_{wCPFRi} = K_{wPi}\boldsymbol{Y}_1(k+N_p) \tag{A.7}$$

where $\boldsymbol{P}_{wCPFRi} = \begin{bmatrix} \Delta P_{wCPFRi}(k+1) \\ \Delta P_{wCPFRi}(k+2) \\ \vdots \\ \Delta P_{wCPFRi}(k+N_p) \end{bmatrix}$.

A.2. Matrix expression

$$\boldsymbol{X}_1\left(k+N_{\mathrm{p}}\right)=\left[\boldsymbol{x}_1(k+1)\quad \boldsymbol{x}_1(k+2)\quad \boldsymbol{x}_1\left(k+N_{\mathrm{p}}\right)\right]^{\mathrm{T}} \tag{A.8}$$

$$\boldsymbol{G}_{x1}=\left[\boldsymbol{G}_1\quad \boldsymbol{G}_1^2\quad \cdots\quad \boldsymbol{G}_1^{N_{\mathrm{p}}}\right]^{\mathrm{T}} \tag{A.9}$$

$$\boldsymbol{H}_{x1}=\begin{bmatrix} \boldsymbol{H}_1 & 0 & \cdots & 0 \\ \boldsymbol{G}_1\boldsymbol{H}_1 & \boldsymbol{H}_1 & \cdots & 0 \\ \boldsymbol{G}_1^2\boldsymbol{H}_1 & \boldsymbol{G}_1\boldsymbol{H}_1 & \cdots & 0 \\ \vdots & \vdots & & \vdots \\ \boldsymbol{G}_1^{N_{\mathrm{p}}-1}\boldsymbol{H}_1 & \boldsymbol{G}_1^{N_{\mathrm{p}}-2}\boldsymbol{H}_1 & \cdots & \boldsymbol{H}_1 \end{bmatrix} \tag{A.10}$$

$$\boldsymbol{D}_1(k)=\left[d_1(k+1)\quad d_1(k+2)\quad \cdots\quad d_1\left(k+N_{\mathrm{p}}\right)\right]^{\mathrm{T}} \tag{A.11}$$

$$\boldsymbol{Y}_1\left(k+N_{\mathrm{p}}\right)=\left[y_1(k+1)\quad y_1(k+2)\quad \cdots\quad y_1\left(k+N_{\mathrm{p}}\right)\right]^{\mathrm{T}} \tag{A.12}$$

$$\boldsymbol{C}_{y1}=\left[\boldsymbol{C}_1\quad \boldsymbol{C}_1\quad \cdots\quad \boldsymbol{C}_1\right]^{T} \tag{A.13}$$

$$\boldsymbol{X}_2\left(k+N_{\mathrm{p}}\right)=\left[\boldsymbol{x}_2(k+1)\quad \boldsymbol{x}_2(k+2)\quad \cdots\quad \boldsymbol{x}_2\left(k+N_{\mathrm{p}}\right)\right]^{T} \tag{A.14}$$

$$\boldsymbol{G}_{x2}=\left[\boldsymbol{G}_2\quad \boldsymbol{G}_2^2\quad \cdots\quad \boldsymbol{G}_2^{N_{\mathrm{p}}}\right]^{T} \tag{A.15}$$

$$\boldsymbol{H}_{x2}=\begin{bmatrix} \boldsymbol{H}_2 & 0 & \cdots & 0 \\ \boldsymbol{G}_2\boldsymbol{H}_2 & \boldsymbol{H}_2 & \cdots & 0 \\ \boldsymbol{G}_2^2\boldsymbol{H}_2 & \boldsymbol{G}_2\boldsymbol{H}_2 & \cdots & 0 \\ \vdots & \vdots & & \vdots \\ \boldsymbol{G}_2^{N_{\mathrm{p}}-1}\boldsymbol{H}_2 & \boldsymbol{G}_2^{N_{\mathrm{p}}-2}\boldsymbol{H}_2 & \cdots & \boldsymbol{H}_2 \end{bmatrix} \tag{A.16}$$

$$\boldsymbol{U}(k)=\left[u(k+1)\quad u(k+2)\quad \cdots\quad u\left(k+N_{\mathrm{p}}\right)\right]^{T} \tag{A.17}$$

$$\boldsymbol{I}_{x2}=\begin{bmatrix} \boldsymbol{I}_2 & 0 & \cdots & 0 \\ \boldsymbol{G}_2\boldsymbol{I}_2 & \boldsymbol{I}_2 & \cdots & 0 \\ \boldsymbol{G}_2^2\boldsymbol{I}_2 & \boldsymbol{G}_2\boldsymbol{I}_2 & \cdots & 0 \\ \vdots & \vdots & & \vdots \\ \boldsymbol{G}_2^{N_{\mathrm{p}}-1}\boldsymbol{I}_2 & \boldsymbol{G}_2^{N_{\mathrm{p}}-2}\boldsymbol{I}_2 & \cdots & \boldsymbol{I}_2 \end{bmatrix} \tag{A.18}$$

$$\boldsymbol{D}_2(k)=\left[d_2(k+1)\quad d_2(k+2)\quad \cdots\quad d_2\left(k+N_{\mathrm{p}}\right)\right]^{T} \tag{A.19}$$

$$\boldsymbol{Y}_2\left(k+N_{\mathrm{p}}\right)=\left[\boldsymbol{y}_2(k+1)\quad \boldsymbol{y}_2(k+2)\quad \cdots\quad \boldsymbol{y}_2\left(k+N_{\mathrm{p}}\right)\right]^{T} \tag{A.20}$$

$$\boldsymbol{E}_{y2}=\left[\boldsymbol{E}_2\quad \boldsymbol{E}_2\quad \cdots\quad \boldsymbol{E}_2\right]^{T} \tag{A.21}$$

$$\boldsymbol{Q}_{\mathrm{Y}}=\begin{bmatrix} \boldsymbol{Q} & & 0 \\ & \ddots & \\ 0 & & \boldsymbol{Q} \end{bmatrix} \tag{A.22}$$

$$\boldsymbol{R}_{\mathrm{U}}=\begin{bmatrix} R & & 0 \\ & \ddots & \\ 0 & & R \end{bmatrix} \tag{A.23}$$

$$\begin{aligned} J(k+1)&=\Psi\left[\boldsymbol{G}_2\boldsymbol{x}^*(k+N|k)+\boldsymbol{H}_2L\left(\boldsymbol{x}^*(k+N|k)\right)\right] \\ &\quad+\sum_{i=1}^{N}\left[\boldsymbol{x}^*(k+i|k)^T\boldsymbol{E}_2^T\boldsymbol{Q}\boldsymbol{E}_2\boldsymbol{x}^*(k+i|k)\right. \\ &\quad\left.+\boldsymbol{u}^*(k+i|k)^T\boldsymbol{R}\boldsymbol{u}^*(k+i|k)\right] \\ &=\sum_{i=0}^{N-1}\left[\boldsymbol{x}^*(k+i|k)^T\boldsymbol{E}_2^T\boldsymbol{Q}\boldsymbol{E}_2\boldsymbol{x}^*(k+i|k)\right. \\ &\quad\left.+\boldsymbol{u}^*(k+i|k)^T\boldsymbol{R}\boldsymbol{u}^*(k+i|k)\right] \\ &\quad+\Psi\left[\boldsymbol{x}^*(k+N|k)\right]+\boldsymbol{x}^*(k+N|k)^T\boldsymbol{E}_2^T\boldsymbol{Q}\boldsymbol{E}_2\boldsymbol{x}^*(k+N|k) \\ &\quad+L\left(\boldsymbol{x}^*(k+N|k)\right)^T\boldsymbol{R}L\left(\boldsymbol{x}^*(k+N|k)\right) \\ &\quad+\Psi\left[\boldsymbol{G}_2\boldsymbol{x}^*(k+N|k)+\boldsymbol{H}_2L\left(\boldsymbol{x}^*(k+N|k)\right)\right] \\ &\quad-\Psi\left[\boldsymbol{x}^*(k+N|k)\right]-\boldsymbol{x}^*(k|k)^T\boldsymbol{E}_2^T\boldsymbol{Q}\boldsymbol{E}_2\boldsymbol{x}^*(k|k) \\ &\quad+-\boldsymbol{u}^*(k|k)^T\boldsymbol{R}\boldsymbol{u}^*(k|k) \\ &=J^*(k)-\boldsymbol{x}^*(k|k)^T\boldsymbol{E}_2^T\boldsymbol{Q}\boldsymbol{E}_2\boldsymbol{x}^*(k|k)-\boldsymbol{u}^*(k|k)^T\boldsymbol{R}\boldsymbol{u}^*(k|k) \\ &\quad+\Psi\left[\boldsymbol{G}_2\boldsymbol{x}^*(k+N|k)+\boldsymbol{H}_2L\left(\boldsymbol{x}^*(k+N|k)\right)\right] \\ &\quad-\Psi\left[\boldsymbol{x}^*(k+N|k)\right] \\ &\quad+\boldsymbol{x}^*(k+N|k)^T\boldsymbol{E}_2^T\boldsymbol{Q}\boldsymbol{E}_2\boldsymbol{x}^*(k+N|k) \\ &\quad+L\left(\boldsymbol{x}^*(k+N|k)\right)^T\boldsymbol{R}L\left(\boldsymbol{x}^*(k+N|k)\right) \end{aligned} \tag{A.24}$$

A.3. Stability analysis

The eigenvalue of the power system integrated with WFs based on CPFR and APFR can be obtained (see Table 1 for the specific values of parameters)

$$\det(s\boldsymbol{I}-\boldsymbol{A}_1)=0 \tag{A.25}$$

$$\det(s\boldsymbol{I}-\boldsymbol{A}_2)=0 \tag{A.26}$$

where $\boldsymbol{I}$ is the identity matrix. According to (A.25) and (A.26), the eigenvalue loci of the two system with F_{H} increasing from 0.15 to 0.4 can be obtained. All of the poles are on the left side of the imaginary axis. The power system integrated with WFs based on CPFR has 3 real poles. For the power system integrated with WFs based on APFR, the real parts of the dominant conjugate poles vary from −0.15 to −0.35, and the absolute value of imaginary parts vary from 0.24 to 0.38. Although the state observer increases the number of poles of the system, according to the separability of the closed-loop pole design in modern control theory, the added poles will not influence the stability of the previous system as long as they are set on the left side of the imaginary axis, and the real part of the added poles are set ten times that of the dominant pole, whose effect can be ignored. Therefore, the stability of the system with different F_{H} is verified.

References

[1] Z. Dong, Z. Li, Y. Dong, S. Jiang, Z. Ding, Fully-distributed deloading operation of DFIG-based wind farm for load sharing, IEEE Trans. Sustain. Energy 12 (1) (2021) 430–440.

[2] K. Elyaalaoui, M. Ouassaid, M. Cherkaoui, Primary frequency control using hierarchal fuzzy logic for a wind farm based on SCIG connected to electrical network, Sustain. Energy Grids Netw. 16 (2018) 188–195.

[3] Y. Ye, Y. Qiao, Z. Lu, Revolution of frequency regulation in the converter-dominated power system, Renew. Sustain. Energy Rev. 111 (2019) 145–156.
[4] B. Bastiani, R. Oliveira, Adaptive MPPT control applied to virtual synchronous generator to extend the inertial response of type-4 wind turbine generators, Sustain. Energy Grids Netw. 27 (2021) 100504.
[5] J. Lee, G. Jang, E. Muljadi, F. Blaabjerg, Z. Chen, Y. Cheol Kang, Stable short-term frequency support using adaptive gains for a dfigbased wind power plant, IEEE Trans. Energy Convers. 31 (3) (2016) 1068–1079.
[6] J. Morren, S.W.H. de Haan, W.L. Kling, J.A. Ferreira, Wind turbines emulating inertia and supporting primary frequency control, IEEE Trans. Power Syst. 21 (1) (2006) 433–434.
[7] Y. Wang, G. Delille, H. Bayem, X. Guillaud, B. Francois, High wind power penetration in isolated power systems—Assessment of wind inertial and primary frequency responses, IEEE Trans. Power Syst. 28 (3) (2013) 2412–2420.
[8] J. Ouyang, M. Pang, M. Li, D. Zheng, T. Tang, W. Wang, Frequency control method based on the dynamic deloading of DFIGs for power systems with high-proportion wind energy, Int. J. Elec. Power 128 (2021) 106764.
[9] G. Ramtharan, J. Ekanayake, N. Jenkins, Frequency support from doubly fed induction generator wind turbines, IET Renew. Power Gener. 1 (1) (2007) 3–9.
[10] K.V. Vidyanandan, N. Senroy, Primary frequency regulation by deloaded wind turbines using variable droop, IEEE Trans. Power Syst. 28 (2) (2013) 837–846.
[11] X. Peng, W. Yao, C. Yan, J. Wen, S. Cheng, Two-stage variable proportion coefficient based frequency support of grid-connected DFIGWTs, IEEE Trans. Power Syst. 35 (2) (2020) 962–974.
[12] Y. Wu, W. Yang, Y. Hu, P.Q. Dzung, Frequency regulation at a wind farm using time-varying inertia and droop controls, IEEE Trans. Ind. Appl. 55 (1) (2019) 213–224.
[13] P. Mahish, A.K. Pradhan, Distributed synchronized control in grid integrated wind farms to improve primary frequency regulation, IEEE Trans. Power Syst. 35 (1) (2020) 362–373.
[14] Z. Wang, W. Wu, Coordinated control method for DFIG-based wind farm to provide primary frequency regulation service, IEEE Trans. Power Syst. 33 (3) (2018) 2644–2659.
[15] C. Jin, W. Li, J. Shen, P. Li, L. Liu, K. Wen, Active frequency response based on model predictive control for bulk power system, IEEE Trans. Power Syst. 34 (4) (2019) 3002–3013.
[16] B. Yang, T. Yu, H. Shu, J. Dong, J. Lin, Robust sliding-mode control of wind energy conversion systems for optimal power extraction via nonlinear perturbation observers, Appl. Energy 210 (2018) 711–723.
[17] P. Kou, D. Liang, L. Yu, L. Gao, Nonlinear model predictive control of wind farm for system frequency support, IEEE Trans. Power Syst. 34 (5) (2019) 3547–3561.
[18] W. Bao, Q. Wu, L. Ding, S. Huang, V. Terzija, A hierarchical inertial control scheme for multiple wind farms with BESSs based on ADMM, IEEE Trans. Sustain. Energy 12 (2) (2021) 751–760.
[19] D. Yang, B. Wang, G. Cai, J. Ma, J. Tian, Z. Chen, L. Wang, Inertiaadaptive model predictive control-based load frequency control for interconnected power systems with wind power, IET Gener. Transmiss. Distrib. 14 (22) (2020) 5029–5036.
[20] L. Ye, C. Zhang, W. Zhong, et al., Hierarchical model predictive control strategy based on dynamic active power dispatch for wind power cluster integration, IEEE Trans. Power Syst. 34 (6) (2019) 4617–4629.
[21] G. Li, H. Ye, Hierarchical nonlinear model predictive control for frequency support of wind farm, Int. J. Elec. Power 129 (4) (2021) 106820.
[22] F. Baccino, F. Conte, S. Grillo, S. Massucco, F. Silvestro, An optimal model-based control technique to improve wind farm participation to frequency regulation, IEEE Trans. Sustain. Energy 6 (3) (2015) 9931003.
[23] A. Ademola-Idowu, B. Zhang, Frequency stability using mpcbased inverter power control in low-inertia power systems, IEEE Trans. Power Syst. 36 (2) (2021) 1628–1637.
[24] J. Liu, Q. Yao, Y. Hu, Model predictive control for load frequency of hybrid power system with wind power and thermal power, Energy 172 (2019) 555–565.
[25] L.A.G. Gomez, L.F.N. Lourenço, A.P. Grilo, M.B.C. Salles, L. Meegahapola, A.J.S. Filho, Primary frequency response of microgrid using doubly fed induction generator with finite control set model predictive control plus droop control and storage system, IEEE Access 8 (2020) 189298-189312.
[26] J. Yang, X. Sun, K. Liao, Z. He, L. Cai, Model predictive controlbased load frequency control for power systems with wind-turbine generators, IET Renew. Power Gener. 13 (15) (2019) 2871–2879.
[27] X. Sun, K. Liao, J. Yang, Z. He, Model predictive control based load frequency control for power systems with wind turbine generators, in: 2019 IEEE Innovative Smart Grid Technologies-Asia (ISGT Asia), Chengdu, China, 2019, pp. 1387–1392.
[28] Technical specification for connecting wind farm to power system-part 1: On shore wind power, GB/T 19963.1-2021, 2021.
[29] P. Kundur, Power System Stability and Control, McGraw-Hill, New York, NY, USA, 1994.
[30] K. Tuttelberg, J. Kilter, D. Wilson, K. Uhlen, Estimation of power system inertia from Ambient Wide Area measurements, IEEE Trans. Power Syst. 33 (6) (2018) 7249–7257.
[31] J. Johnson, J.C. Neely, J.J. Delhotal, M. Lave, Photovoltaic frequency–watt curve design for frequency regulation and fast contingency reserves, IEEE J. Photovolt. 6 (6) (2016) 1611–1618.
[32] P.M. Anderson, M. Mirheydar, A low-order system frequency response model, IEEE Trans. Power Syst. 5 (3) (1990) 720–729.
[33] J.M. Mauricio, A. Marano, A. Gomez-Exposito, J.L. Martinez Ramos, Frequency regulation contribution through variable-speed wind energy conversion systems, IEEE Trans. Power Syst. 24 (1) (2009) 173–180.
[34] W. Kwon, A. Pearson, On feedback stabilization of time-varying discrete linear systems, IEEE Trans. Automat. Control 23 (3) (1978) 479481.
[35] J.W. Lee, W.H. Kwon, J. Choi, On stability of constrained receding horizon control with finite terminal weighting matrix, Automatica 34 (12) (1998) 1607–1612.
[36] D.Q. Mayne, j.b. Rawlings, C.V. Rao, P.O.M. Scokaertc, Constrained model predictive control: Stability and optimality, Automatica 36 (6) (2000) 789–814.
[37] X. Lyu, Y. Jia, Z. Xu, A novel control strategy for wind farm active power regulation considering wake interaction, IEEE Trans. Sustain. Energy 11 (2) (2020) 618–628.
[38] Y. Li, Z. Xu, J. Zhang, H. Yang, K.P. Wong, Variable UtilizationLevel scheme for load-sharing control of wind farm, IEEE Trans. Energy Convers. 33 (2) (2018) 856–868.
[39] P.W. Sauer, M.A. Pai, Power System Dynamics and Stability, Prentice-Hall, Upper Saddle River, NJ, 1998.
[40] G.P. Prajapat, N. Senroy, I.N. Kar, Stability enhancement of dfigbased wind turbine system through linear quadratic regulator, IET Gener. Transmiss. Distrib. 12 (6) (2018) 1331–1338.
[41] M.H. Ravanji, C.A. Canizares, M. Parniani, Modeling and control of variable speed wind turbine generators for frequency regulation, IEEE Trans. Sustain. Energy 11 (2) (2020) 916–927.